ACS APPLIED MATERIALS & INTERFACES

www.acsami.org

Research Article

High Mobility, Low Off-Current, and Flexible Fiber-Based a-InGaZnO Thin-Film Transistors toward Wearable Textile OLED Displays

Chan Young Kim, Yong Ha Hwang, Jaehyeock Chang, Seong Uk Kong, Sang-Hee Ko Park, and Kyung Cheol Choi*

Cite This: *ACS Appl. Mater. Interfaces* 2024, 16, 62335−62346

Read Online

ACCESS | Metrics & More | Article Recommendations | Supporting Information

ABSTRACT: Fiber-based organic light-emitting diodes (OLEDs) are gaining attention as promising candidates to achieve truly wearable textile displays because of their favorable electrical and mechanical characteristics. However, although fiber OLEDs have been developed into passive-matrix displays, it has not been possible to achieve active OLED operation because of the difficulty of realizing fiber-based thin film transistors (TFTs) with the proper electrical and mechanical performance at the same time. Here, 1D cylindrical fiber-based IGZO TFTs, which simultaneously exhibit a high electrical performance and flexibility, are reported. To address this trade-off relationship, four key stages of a novel fabrication process and unique device structures that suitable for the thermal properties and cylindrical structure of the fiber were applied: (I) prethermal treatment, (II) partially patterned layers, (III) coplanar structure, and (IV) continuous postannealing (CPA) process. As a result, the fabricated fiber-based IGZO TFTs showed high mobility (8.6 cm^2/(V s)) and low off-current (~10^{-12} A), comparable to that glass-based TFTs, as well as flexibility. Furthermore, based on these valid performances, it was demonstrated that fiber phOLEDs could be driven by fiber-based IGZO TFTs using a wiring connection with Cu wire and Ag paste. The results suggest that this may allow the potential fabrication of fully textile AMOLED displays, integrated with TFTs.

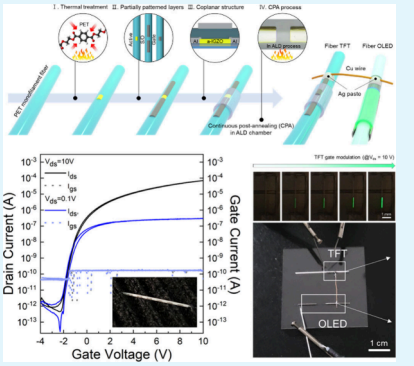

KEYWORDS: *fiber-based thin-film transistors, low temperature process, flexible thin-film transistors, fibertronics, textile display, wearable display*

1. INTRODUCTION

Wearable textile displays (WTDs) have attracted considerable attention as promising candidates for human-friendly wearable displays. WTD can efficiently transmit information by direct contact with the human body while offering the natural characteristics of textiles, such as free-deformity, portability, wearability, and light weight.[1−5] The technology is expected to develop multifunctional and multipurpose utility using hyper-connections, for display and sensing functions and electronic textiles (e-textile), as well as wearable electronics in the form of accessories like smart watches.[6−13] In particular, because they consist of distinct cylindrical structured fibers and are flexible in all directions, textiles woven from the 1D cylindrical fibers provide outstanding 3D free-deformity characteristics natural to textiles.[4,14] To maximize the advantage of these features, many research groups have developed electronics based on fiber (fibertronics), such as transistors,[10,12,13,15−17] sensors,[18,19] batteries,[20,21] energy devices,[22,23] circuits,[24,25] and light-emitting devices.[2,3,11,26−28]

Meanwhile, in the display industry, active-matrix organic light emitting diode (AMOLED) displays, enabled by thin film transistors (TFTs) with high mobility and low off-current, have become a leading technology. Compared with passive-matrix type displays, they offer low power consumption and internal compensation technologies that enable high resolution and a thin panel.[26] To date, fiber-based displays have followed the sequence of development of other display technologies, moving from light source development to a passive matrix.[2,29,30] In particular, fiber OLED technologies, which are also considered to be strongly suitable for textile displays because of their low driving voltage, flexibility, and high performance, have reached maturity as passive matrix displays.[31] Like display technologies in the display industry, the direction of technological development of fiber-based displays is clear. Therefore, to achieve fiber-based displays with active operation, low power consumption, and high resolution, it will be necessary to develop flexible fiber-based thin film transistors (TFTs) with the level of mobility used in the industry (>8−10 cm^2/(V s)), as well as low off-current.

With this goal in mind, numerous research groups have developed fiber-based TFTs using various active materials,

Received: July 22, 2024
Revised: October 23, 2024
Accepted: October 25, 2024
Published: October 30, 2024

https://doi.org/10.1021/acsami.4c12223
ACS Appl. Mater. Interfaces 2024, 16, 62335−62346

Table 1. Electrical Performance of HLF TFTs Based on Glass and PET Fiber

substrate	V_{th} (V)	μ_{sat} ($cm^2/(V\ s)$)	SS (mV/dec)	on/off ratio
flat glass	−2.0 ± 0.17	9.4 ± 0.4	131 ± 12	$[3.02(\pm2.5)] \times 10^8$
PET fiber	−2.3 ± 0.15	8.6 ± 0.6	201 ± 20	$[7.05(\pm3.5)] \times 10^7$

Table 2. Comparison of Reported Fiber TFTs

device type	active material	gate insulator material	fiber type	mobility ($cm^2/(V\ s)$)	off state current (A)	on/off ratio	bending test	func	ref
WECTs	electrolyte containing 33 wt % PSS, 12 wt % glycol, etc.	polyamide monofilament	N/A	$\sim10^{-7}$	$\sim10^{3}$	N/A	N/A		62
	electrolyte (ionic liquid and polymer ionic liquid)	silk fiber	N/A	$\sim10^{-8}$	$\sim10^{2}$	N/A	N/A		63
organic TFTs	pentacene	cross-linked PVP	Al, stainless steel wires	10^{-2}	10^{-2}	N/A	N/A		64
	pentacene	PVCN	Al wire	0.53	10^{-9}	4×10^3	∼0.9%		16
	diF-TESADT with PMMA	PMMA	Au microfiber	0.2	10^{-11}	$\sim10^4$	∼1.6%		13
	P3HT	SiO_2	TPU, graphene/Ag hybrid fiber	1.92	10^{-8}	$\sim10^4$	N/A		65
	P3HT, P3HT-NR	ion-gel	Au microfiber	0.2	10^{-7}	10^4−10^5	2R		12
SWCNT TFTs	patterned SWCNT (p-type)	Al_2O_3	optical fiber	4.03	$\sim10^{-10}$	10^4−10^5	N/A	CMOS	17
	SWCNT doped with N-DMBI (n-type)	Al_2O_3	optical fiber	2.15	$\sim10^{-8}$	$\sim10^3$	N/A		17
oxide TFTs	solution processed IGZO	AlO_x	glass optical fiber	3.7	10^{-11}	$\sim10^6$	N/A		15
	sputtered IGZO	Al_2O_3−MgO nanolaminate	glass fiber	3.46	10^{-13}	5.73×10^8	N/A		10
	sputtered IGZO	**Al_2O_3**	**PET fiber**	**8.6**	**$\sim10^{-12}$**	7.05×10^7	**0.6%**	**with fiber OLED**	**this work**

such as organic materials,[12,13,16] single-walled carbon nanotubes (SWCNTs),[17] and metal oxide semiconducting materials.[10,15,32,33] The organic field-effect transistors (OFETs) have shown excellent flexibility, and a woven TFT array, and a transistor with a new architecture, have been proposed.[12,13,16,17] However, while the structural limitations of the 1D cylindrical fiber structure have been overcome, OFETs typically exhibit poor electrical performance, with high leakage current, low on/off ratio, and low mobility of <1−2 $cm^2/(V\ s)$. The limited performance is attributed to the low-temperature solution process used to fabricate the fibers, which results in residual solvents that adversely affect performance. At the same time, a CMOS inverter circuit has been proposed based on p- and n-type TFTs based on SWCNTs and exhibited mobilities of 4.03 and 2.15 $cm^2/(V\ s)$ on an optical fiber.[17] There have also been cases where In−Ga−Zn−O-based metal oxide FETs have been manufactured using a solution process with a dip coating method on glass optical fibers[15] or partially patterned and vacuum deposited all layers on glass fibers in our previous work,[10] all of which have a mobility of >3 $cm^2/(V\ s)$ and an on−off ratio >10^6. The SWCNTs and oxide-based FETs showed improved electrical performance. However, despite the remarkable breakthrough in terms of the device performance and functions, flexibility could not be confirmed because they were fabricated on glass fibers.

In previous studies of fiber-based TFTs, a trade-off relationship between electrical and mechanical properties has been clearly observed. Hard substrates are advantageous at high temperatures, being robust to thermal variables and still delivering high performance, but they are not flexible. The opposite is true for flexible substrates. To resolve this relationship, our previous research tried to prepare oxide-based TFTs on flexible cylindrical PET fibers.[32,33] However, there was a lack of understanding of the thermal aspects of the fabrication process and its effect on the flexible PET fiber substrate and the lack of consideration for a suitable device structure regarding the cylindrical substrate. As a result, suitable performance and characteristics, such as stable electrical properties, bending properties, and high reproducibility, were not guaranteed.

The present study developed high mobility, low off-current, and flexible fiber-based IGZO TFTs (HLF fiber TFTs) capable of overcoming the trade-off relationship between electrical and mechanical properties. The HLF fiber TFTs were fabricated on 1D cylinder-shaped PET synthetic fiber that has been actually actively used under the name "polyester" in the clothing and textile industries. The HLF fiber TFTs were successfully implemented by applying four key stages, which simultaneously achieved electrical and mechanical properties. These steps were (I) prethermal treatment, (II) partially patterned layers, (III) coplanar structure, and (IV) continuous postannealing (CPA) process. The HLF fiber TFTs fabricated in this way showed an electrical saturation mobility of 8.6 $cm^2/(V\ s)$, a subthreshold slope (SS) of 201 mV/dec, and an on/off ratio of 7.05×10^7, comparable to those of the glass-based TFTs. Flexibility was confirmed, using 0.6% strain in a 1000 cycle tensile bending test. The a-IGZO's unique advantages[34−37] include high mobility (>8−10 $cm^2/(V\ s)$) and low leakage current and were simultaneously implemented in 1D cylindrical flexible fibers with flexibility. In addition to the achieved low off current ($\sim10^{-12}$ A), the saturation mobility of 8.6 $cm^2/(V\ s)$, a valid level of mobility used in the industry, is also the highest mobility value among the results reported thus far, as shown in Tables 1 and 2. To demonstrate the integration of the HLF fiber TFTs with the OLEDs, a green fiber phOLED was successfully driven by the HLF fiber TFTs using a simple connection, consisting of the fiber phOLED, the

https://doi.org/10.1021/acsami.4c12223
ACS Appl. Mater. Interfaces 2024, 16, 62335−62346

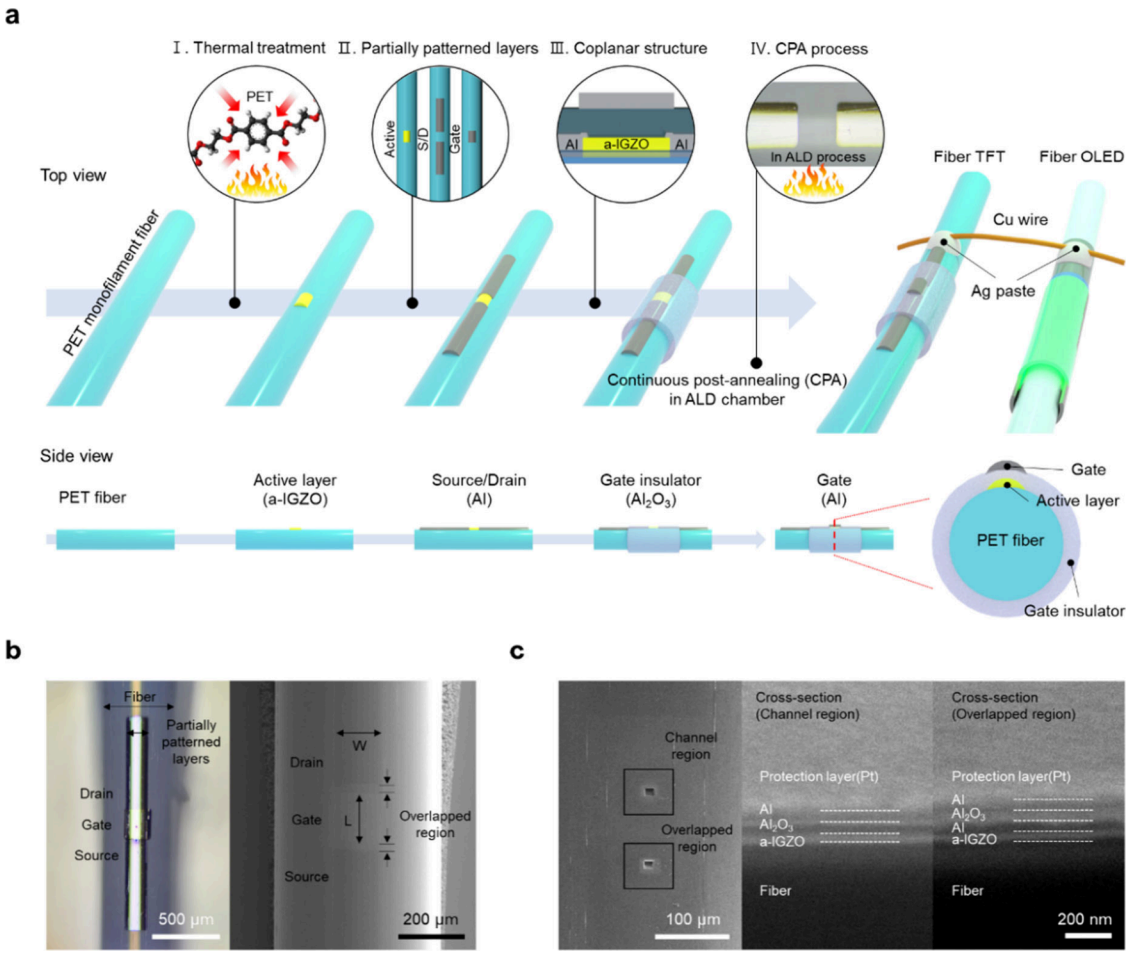

Figure 1. Schematic illustration of the structures of the thin film transistors. (a) Schematic illustration of the HLF-fiber TFT fabrication process with four key stages: (I) prethermal treatment, (II) partially patterned layers, (III) coplanar structure, and (IV) continuous postannealing (CPA) process. (b) Optical microscopy image (left) and top-view SEM image of HLF-fiber TFT. (c) Magnified top view SEM image of the HLF-fiber TFT (left), cross-sectional SEM image of the HLF-fiber TFT on the PET fiber, in the channel region (middle) and overlapped region (right).

HLF fiber TFTs, and Cu wire, which were bonded with commercial silver paste.

2. RESULTS AND DISCUSSION

Figure 1a presents the entire fabrication process with the four key stages (I–IV) for realizing the HLF fiber TFTs and cross-sectional views. The four key stages are composed of an essential novel fabrication process and unique device structures to successfully realize HLF fiber TFTs on a flexible 1D cylindrical shaped PET fiber, achieving good electrical performance comparable to that of TFTs fabricated on flat glass. (I) shows the prethermal treatment, for thermal stabilization and to improve the roughness of the PET substrate by increasing the orientation of the polymer chains and crystallization. (II) is a partially patterned layer technique, utilizing conventional vacuum deposition, which can provide reliability, enabling stable and reliable electrical properties in the cylindrical fibers. (III) shows a top-gate coplanar structure which is suitable for fiber-based TFTs. It can improve the non-Ohmic contact issue at the interface of the source/drain and an active layer, induced by plasma damage during the rf sputtering. (IV) is a continuous postannealing (CPA) step consisting of continuous thermal treatment in vacuum conditions after forming a gate insulator in a thermal ALD (atomic layer deposition) chamber and thermal consideration. The effect of each step will be discussed in detail later.

The last representative scheme in Figure 1a illustrates that the HLF fiber TFT made with the four key stages is connected with the fiber phOLED using Cu wire and Ag paste, showing the drive scheme consisting of the fiber phOLED and fiber TFT. Figure 1b shows an optical microscopy (OM) photograph (left) and a scanning electron microscopy (SEM) image (right) of the HLF fiber TFT fabricated on a 500 μm thick PET fiber. The source/drain and active layer regions were partially patterned on PET fiber, and the channel dimensions (i.e., channel length (L: ~140 μm) and width (W: ~140 μm)) of the HLF fiber TFT with a top-gate coplanar structure and active layer and source/drain overlapped areas (~10 μm) are shown. The HLF fiber TFT consists of a channel region, a channel-source/drain overlapped region, and a source/drain region; the three different parts were successfully stacked with thin films. The channel region is a-IGZO/Al_2O_3/Al, the overlapped region is a-IGZO/Al/Al_2O_3/Al, and the source/drain region is composed of a single deposited Al thin film. Figure 1c shows a magnified SEM image of the HLF fiber TFT and its cross-sectional view, confirming the thickness of the layers in the zone described above, using a focused ion beam (FIB) system: a-IGZO (~50 nm), Al_2O_3 (~60 nm), and Al (~50 nm).

https://doi.org/10.1021/acsami.4c12223
ACS Appl. Mater. Interfaces 2024, 16, 62335−62346

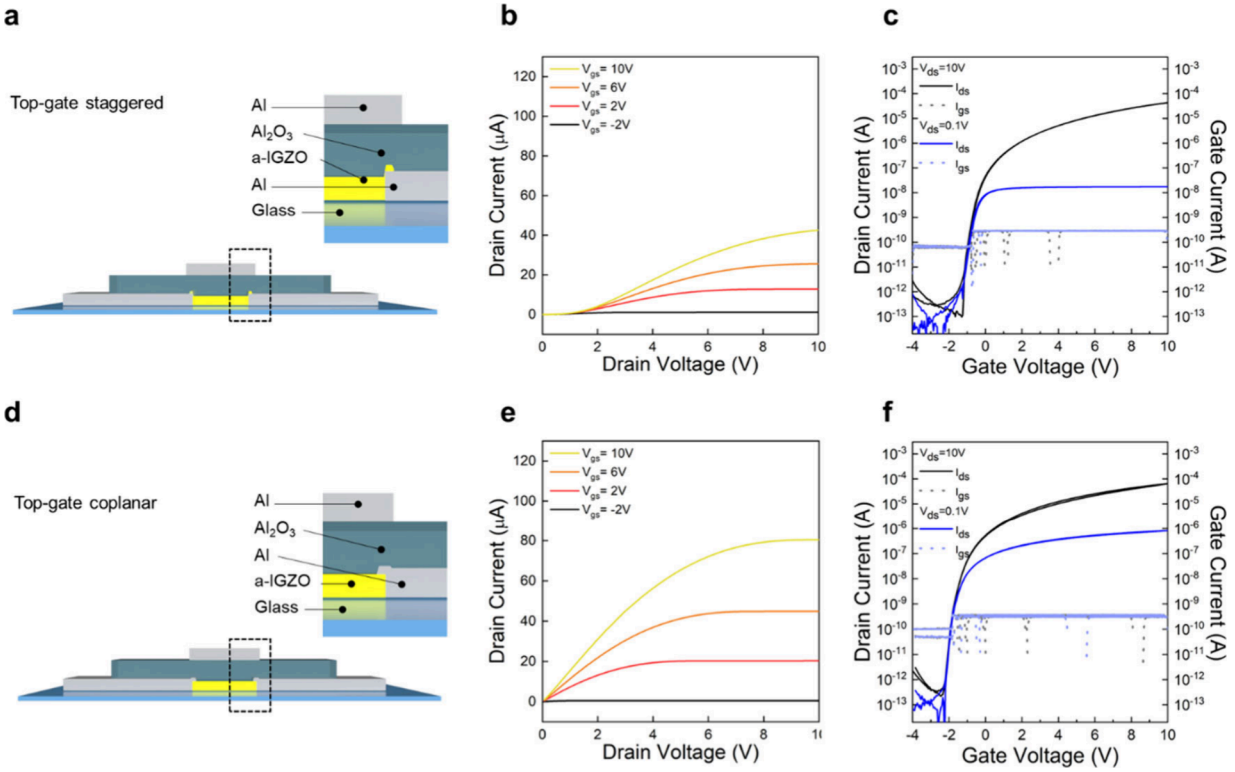

Figure 2. (a) Schematic illustration of the top-gate staggered structure of the HLF TFT based on glass. (b, c) Output (I_{DS}−V_{DS}) (b) and transfer (I_{DS}−V_{GS}) (c) characteristics of the top-gate staggered structure HLF TFT. (d) Schematic illustration of top-gate coplanar structure of the HLF TFT based on glass. (e, f) Output (I_{DS}−V_{DS}) (e) and transfer (I_{DS}−V_{GS}) (f) characteristics of the top-gate coplanar structure HLF TFT.

Figure 2a−f shows the justification for selecting a top-gate coplanar structure (the key stage (III)) suitable for HLF TFTs fabricated on a PET fiber. The top-gate structure was chosen as the suitable TFT structure for the fiber device. It was known that the advantage of the top-gate structure is that the gate dielectric layer can act as a passivation layer by covering the channel layer. In particular, the Al_2O_3 gate dielectric layer formed by the ALD showed excellent performance, passivating H_2O and H_2. Furthermore, a film with uniform thickness can be formed with excellent step coverage on a cylindrical shaped substrate.[38] In other words, without additional encapsulation layers, the IGZO channel layer partially patterned on the cylindrical shaped fiber can be stably protected from the external environment. Meanwhile, the contact resistance limits the injected current and decreases the voltage drop across the channel.[39,40] For this reason, a coplanar structure was selected. In the case of a top-gate staggered structure, where the IGZO channel layer is deposited by rf sputtering after the formation of the Al electrode, a contact issue occurs due to surface damage caused by plasma during the rf sputtering IGZO deposition.[41,42] To address this, a coplanar structure that forms a channel first was applied like LTPS TFTs.[43,44] The Ohmic effect can simply confirm whether the drain current exhibits a linear regime in the low drain voltage section of the output characteristics, and was clearly extracted using the channel-length-scaling method for different gate voltage biases.[45,46] Figure 2a,d presents schematic diagrams of the glass-based TFTs, which were fabricated with a top-gate staggered structure and a top-gate coplanar structure, respectively. Figure 2b,c shows the evaluation of the electrical output and transfer characteristics of the top-gate staggered structure, respectively. In Figure 2b, non-Ohmic characteristics with nonlinear regime were observed in the linear region and low drain voltage range. On the other hand, in Figure 2e, Ohmic characteristics with a linear regime in the linear region were observed, unlike in Figure 2b. In addition, a difference in drain current was observed according to the gate voltage sweep of V_{DS} = 10 V and V_{DS} = 0.1 V. It occurred less in Figure 2f than in Figure 2c. The results show the current reliability of the device with different drain voltage biases due to the influence of the contact resistance issue.

Figure 3a and Figures S1 and S2 explain the effect of thermal stabilization and reduced roughness of the PET fiber through prethermal treatment (the key stage (I)). A PET can be thermoformed by the heat distortion temperature (HDT). Through the heat treatment heat resistance can increase as the orientation of the polymer chains and crystallization are increased by the proper thermal treatment range and heating rate. In particular, on heat treatment in the range of >150 °C, PET undergoes extreme thermal distortion and contraction.[47,48] Thus, the aging, which is the prethermal treatment, was performed by heating the PET fiber at 150 °C for 10 min (the key stage (I)). After prethermal treatment, it was confirmed that the PET fiber was thermally contracted and thermally stable (Figure S1). As shown in Figure S2, through preannealing it is possible to prevent misalignment which can greatly affect device performance during the subsequent active layer thermal treatment step (at 150 °C). Furthermore, as shown in Figure 3a, the root-mean-square roughness (R_{rms}) can be improved, resulting in a planarization effect. To ensure the performance of TFTs manufactured by thin film deposition (<100 nm), it is essential to form uniform thin films as layers with as low an R_{rms} as possible. In addition, the top-gate structure, where the surface of the back channel is formed by

https://doi.org/10.1021/acsami.4c12223
ACS Appl. Mater. Interfaces 2024, 16, 62335−62346

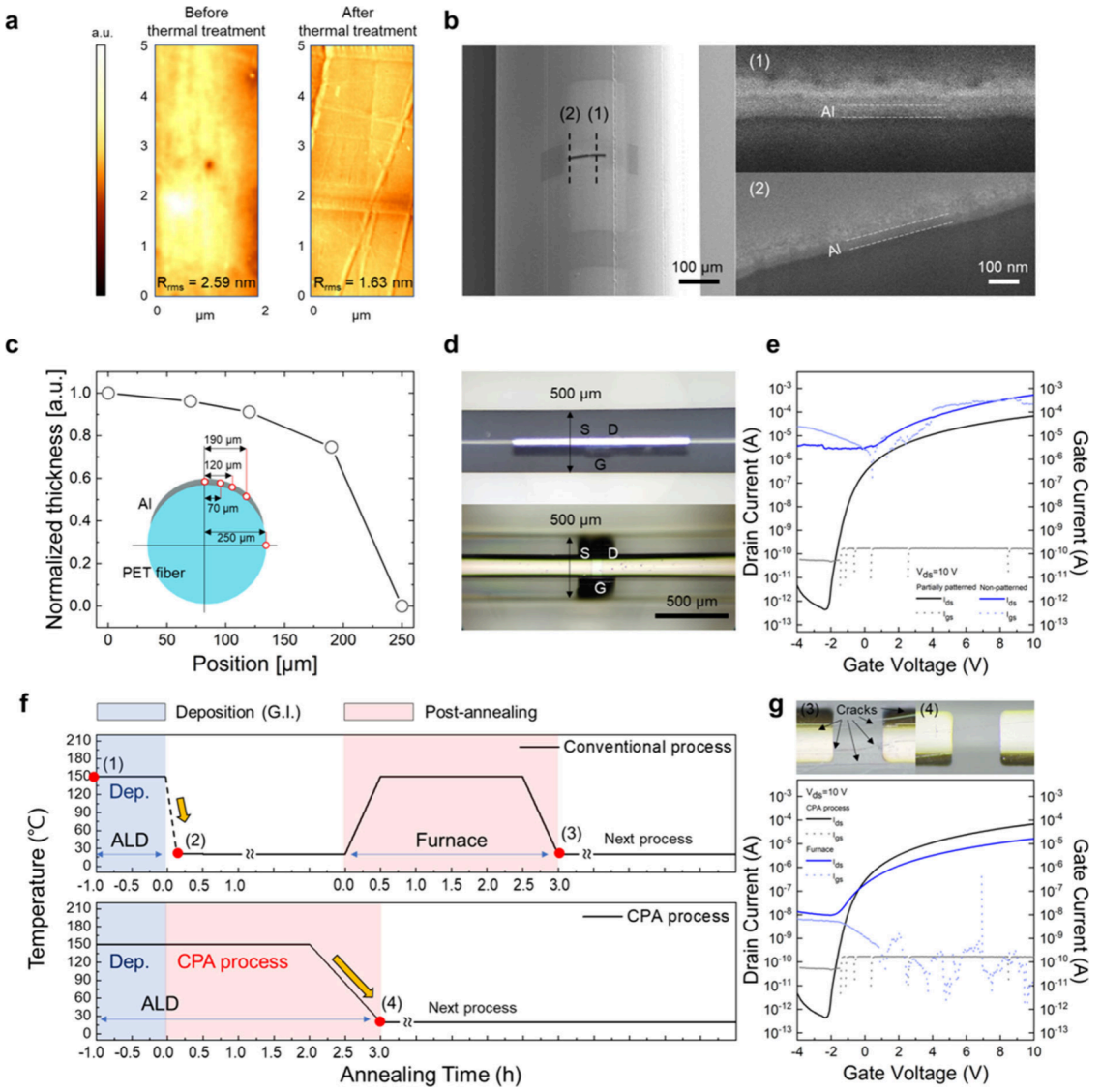

Figure 3. (a) AFM images of morphology before and after prethermal treatment of the PET fiber. (b) Magnified top-view (left) and cross-sectional (right) SEM images of the source/drain region on the PET fiber (left) and cross-sectional SEM images of the source/drain region. (c) Normalized thickness of the single side deposited Al thin film versus position of PET fiber. (d, e) Optical microscopy images (d) and transfer characteristics (e) to compare the electrical performance of a partially patterned HLF-fiber TFT on 500 μm and fully patterned HLF-fiber TFT on 500 μm diameter PET fiber (blue curves, nonpatterned; black curves, partially patterned). (f) Annealing temperature versus annealing time to compare the CPA process and conventional TFT process. (g) The surface state of the source/drain and active region of HLF-fiber TFT according to each point (3,4) in (f) and transfer curves to compare their electrical performance (blue curves, conventional process; black curves, CPA process).

direct contact with the substrate, can be greatly affected by the surface roughness. Poor surface roughness creates scattering centers with charge trap sites that interrupt the transport of accumulated electrons.[49,50] Thus, key stage (I) was established to prevent the higher off-current and lower mobility that results from a rough surface as well as misalignment.

Unlike a 2D film, which can be easily formed into a uniform thin film, on a cylindrical shaped fiber, it can be challenging to form a thin film with an optimized width, because of the curvature and diameter of the fiber. Figure 3b–e explains the partially patterned layer technique (the key stage (II)) that was used to fabricate the HLF fiber TFTs on cylindrical shaped fibers. The resulting fibers exhibited stable and reliable electrical performance. Figure 3b presents a top view (left) of the 50 nm thick Al source/drain with a width of 140 μm, which was formed on the 500 μm diameter PET fiber, and a cross-sectional SEM image (right) showing the thickness of the Al thin film relative to the position of the fiber: (1) ~50 nm, (2) ~47 nm. To suppress nonuniformity in the thin film, which can cause deterioration of device performance, all of the layers except the gate insulator were patterned with a width equal to approximately 30% of the fiber diameter. In Figure 3c and Figure S3, the thickness of the film at each position was ensured by depositing 50 nm thick Al on the surface of the 500 μm diameter PET fiber from the middle region to the side region in the normal direction. Based on the results, the width of the patterned layers was determined to be 120 μm and there was no significant difference in thickness at the center. To confirm the effect of the uneven film, partially patterned and nonpatterned HLF fiber TFTs were fabricated on 500 μm thick PET fibers, respectively (Figure 3d). Figure 3e demonstrates that unevenness affects the performance,

https://doi.org/10.1021/acsami.4c12223
ACS Appl. Mater. Interfaces 2024, 16, 62335−62346

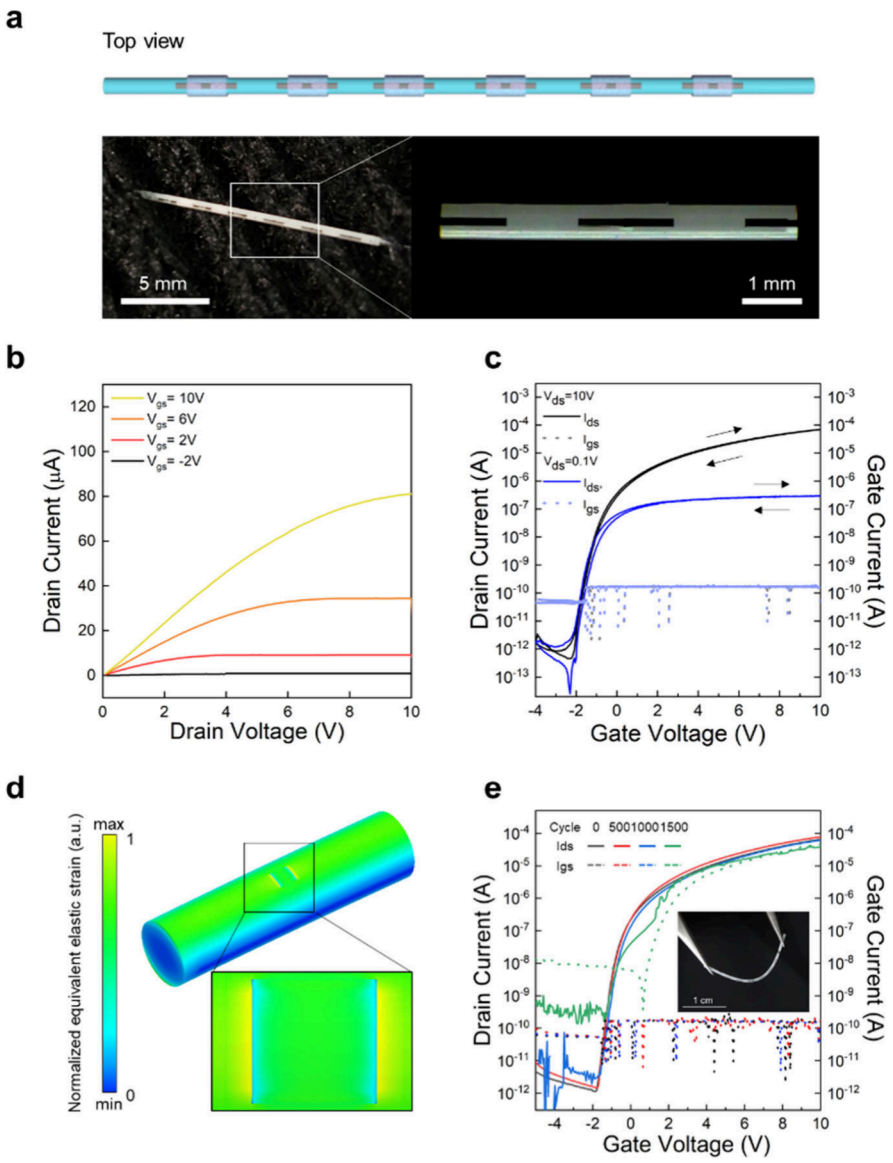

Figure 4. (a) Top view schematic illustration (top), photograph of the textile-embedded HLF-fiber TFTs (left), and a magnified optical microscopy image (right) of the HLF-fiber TFTs. (b, c) Output (I_{DS}−V_{DS}) (b) and transfer (I_{DS}−V_{GS}) (c) characteristics of the HLF-fiber TFT. (d) ANSYS simulation result for the distribution of the equivalent elastic strain in the cross-section of the IGZO/Al_2O_3 thin film deposited on a PET fiber in a 0.6% tensile bending test. (e) Transfer characteristics of the HLF-fiber TFTs with increasing bending cycles under a 0.6% tensile strain condition at V_{DS} = 10 V (inset: photograph of the bent HLF-fiber TFTs).

showing strongly degraded transfer characteristics compared with the proposed HLF fiber TFTs. When manufacturing a nonpatterned HLF fiber TFT on a 500 μm thick PET fiber, the TFT is produced as a layer close to the entire surface deposition. Due to the uneven formation of the thin films on the PET fiber, an error for the invalid channel region occurs, meaning that the mobility, off-current (leakage current), on-current, and SS are all noticeably deteriorated.

Figures 3f,g are presented to help explain the CPA process (the key stage (IV)) which is a novel postannealing method considering the thermal effect. Conventional metal oxide TFTs require an additional postannealing to improve the film quality of the channel layer and the interface issue of the channel layer/gate dielectric layer and to remove surface and internal trap sites from the channel layer.[38] As mentioned above, due to the thermal deformation properties of PET, the postannealing process was performed at 150 °C. As shown in the conventional process graph in Figure 3f, an additional annealing step was performed separately from the thin film deposition step, which induces additional environmental variables such as thermal changes and atmosphere. It is known that various mechanical properties, including tensile modulus, yield stress, and the fracture toughness of semi-crystalline polymeric materials such as PET, can be changed depending on the cooling rate. In particular, fast-cooled polymeric materials show considerably more internal cracking and delamination than slow-cooled polymers, and these damages are likely due to the large thermal strains induced by the fast cooling process.[51,52] Figure S4 shows the results of thermomechanical analysis (TMA), which was performed using 500 μm thick PET fiber through no postannealing and furnace and CPA processes at 150 °C for 2 h, glass transition (T_g) of the PET fiber thermally annealed through the furnace and CPA process showing a difference of 12 °C, which is the

https://doi.org/10.1021/acsami.4c12223
ACS Appl. Mater. Interfaces 2024, 16, 62335−62346

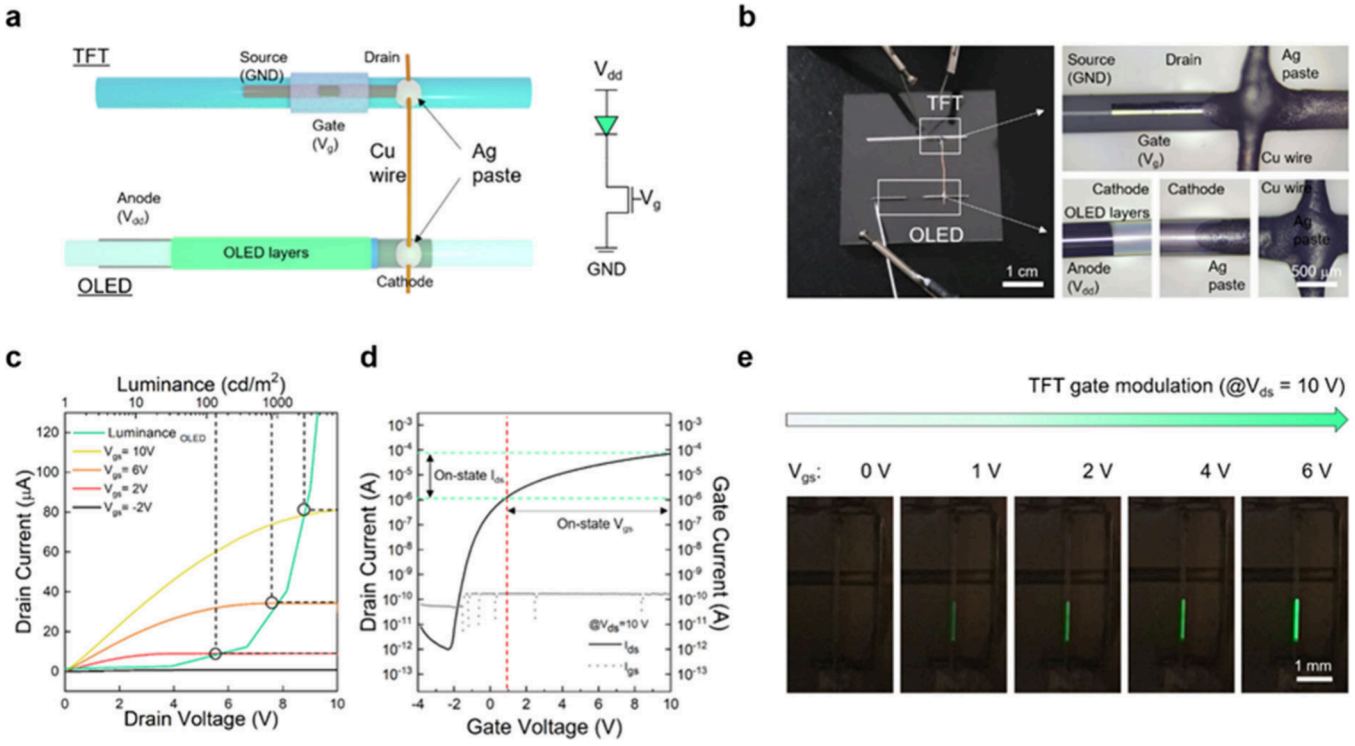

Figure 5. (a) Schematic illustration of the metal wiring contact method used to drive the fiber phOLED with the HLF-fiber TFT. (b) Photograph (left) and magnified optical microcopy images of the components (right) of the proposed metal wire contacted HLF-fiber TFT and fiber phOLED. (c) Luminance versus drain current curves in the output characteristics of the fiber phOLED controlled by the HLF-fiber TFT. (d) Transfer characteristics of the HLF-fiber TFT with I_{DS} and V_{GS} range of on-state of the fiber phOLED. (e) Photograph of changing emission intensity of the fiber phOLED according to gate modulation of the HLF-fiber TFT (I_{DS} = 3.123 × 10^{-7} A at V_{GS} = 0 V, I_{DS} = 1.394 × 10^{-6} A at V_{GS} = 1 V, I_{DS} = 2.537 × 10^{-5} A at V_{GS} = 6 V).

same as the trend of previous research results related to the fast cooling process. Thus, although very little thermal deformation occurs when an additional annealing step is performed below the specific temperature at which PET was formed, this phenomenon remains an important issue to be considered, since it can affect the layers of the TFT formed on the surface of the 500 μm thick PET fiber.[53] In the CPA process, thermal treatment is continuously performed in the ALD chamber after the gate insulator deposition from the ALD, unlike the conventional process. This provides a strong advantage, in that the cooling process is performed only one time, compared to two times in the conventional process. This reduces the effect of environmental variables such as thermal changes and the atmosphere. Furthermore, after thermal treatment in the ALD chamber, damage to the thin films can be minimized by extending the cooling time to 1 h without the temperature fluctuation, by setting a set point. Figure 3g confirms that the CPA process, which controls the cooling process and the environments, is essential for the PET fiber-based TFTs. The surface states of the source/drain and active regions of the HLF fiber TFTs before and after thermal treatment are shown in Figure 3g. With rapid cooling after thermal treatment, cracks occurred on the surface of the PET fiber, which directly damaged the structure of the HLF fiber TFTs, and in particular, seemed to be the main cause of the broken active layer and gate insulator. On the other hand, with an optimized cooling rate after the CPA process, cracks were not generated on the surface of the PET fiber, which formed stably and appeared to be the same as the structure before the thermal treatment, resulting in high mobility and low off-state current (Figure 3g and Figure S5). In several previous studies including our previous works, the primary reason TFTs were not implemented on flexible polymeric fibers seems to be that there was no consideration of thermal conditions or the use of thermal treatment equipment, such as furnaces, where the cooling rate cannot be controlled, resulting in fluctuating temperatures. Accordingly, a postannealing method that can control the cooling process, such as the CPA process, should be included in the fabrication process of the flexible fiber TFT.

Figure 4a shows a top view illustration and OM image of the HLF fiber TFTs that were successfully fabricated on 500 μm diameter PET. As shown in the top view illustration in Figure 4a, multiple TFTs were fabricated on one strand of PET fiber to achieve the aforementioned design. Figure 4b shows the Ohmic characteristics with a linear regime in the linear region of the contact issue at the IGZO/Al interface by applying the top-gate coplanar structure on the PET fiber. The transfer characteristics in Figure 4c were measured under the conditions of V_{DS} = 0.1−10 V and the hysteresis performance at each V_{DS} is presented to show the electrical reliability of the device. It can be seen that the HLF fiber TFTs exhibited excellent electrical performance, comparable to those of the TFTs fabricated on flat glass, and demonstrated the level of performance required for active-type displays. (Table 1) In particular, the saturation mobility of 8.6 $cm^2/(V\ s)$ is the highest reported mobility value among results thus far (Table 2). This mobility can produce a high-resolution FHD display with a frame rate of 240 Hz or higher.[54] The high reproducibility of the electrical performance of the HLF fiber TFTs was demonstrated by showing the transfer characteristics

https://doi.org/10.1021/acsami.4c12223
ACS Appl. Mater. Interfaces 2024, 16, 62335−62346

of the HLF fiber TFTs fabricated on different days in Figure S6. However, when compared to HLF TFTs fabricated on flat glass, the saturation mobility showed very little deterioration, of less than 9%, from 9.4 to 8.6 $cm^2/(V\ s)$. Considering the difference in performance, this slight electrical deterioration can be attributed to the aforementioned R_{mrs} of 1.63 nm of the PET fiber substrate and the IGZO-channel layer thickness uniformity issue, which affects the carrier concentration inside the channel, shown in Figure 4b,c. To further investigate the causes, a qualitative analysis was performed (Figures S7 and S8). In Figure S8, the XPS profile analysis confirmed that C−C bonding was found in the IGZO back channel (etching time = 360 s). This proved that carbon had diffused into the IGZO back channel from the PET.[55] Several previous studies have reported that a carbon impurity or defect can act as a trap in the channel. It has also been reported that such carbon diffusion can cause V_{th} shift as well as deterioration of electrical performance, thereby affecting the reliability of the device.[56−59]

Figure S9 shows the results of the positive bias stress (PBS) and negative bias stress (NBS) tests for the HLF fiber-based TFT, highlighting the need to enhance the reliability of the V_{th} shift characteristics of the device. The application of a bottom encapsulation layer serves as a viable alternative to protect the back channel from defect outgassing from PET fibers as well as carbon diffusion.

Figure 4d shows the results of a mechanical simulation performed to predict and explain the flexibility characteristics of the HLF fiber TFTs. Since Al_2O_3 is commonly known to fail at ∼0.6% tensile strain,[60,61] the tensile strain distribution of 0.6% was applied to the 140 μm × 140 μm partially patterned 40 nm thick IGZO, and the 60 nm thick Al_2O_3 structure deposited on 500 μm diameter PET fiber was examined. The results confirmed that the largest strain occurred in the gap between the thin films and the largest strain was expected to first occur at the gap. Figure 4e shows the result of the transfer characteristics according to the number of cycles to show the results of the 0.6% tensile strain bending test based on the simulation result. A photograph of the tensile bending test system and illustration to explain the elements of the HLF-fiber TFTs for calculating the tensile strain are presented in Figure S10. Like the simulation, the results confirmed that an increase in gate leakage occurred when the gate insulator on the edge was broken after 1500 cycles. Meanwhile, the off-current also gradually increased. The mechanical cracks were induced by bending tensile stress which caused an increase in off-current.[61] It was confirmed that this also affects the physical properties of the thin film, as observed in the O 1s XPS spectra before and after the application of 0.6% tensile strain to the HLF TFT on the PET substrate (Figure S11). In the control group, the characteristics of the components without undergoing the CPA process were examined before and after bending, and an increase in the off-current was observed (Figure S12). Furthermore, as is commonly known, the cylindrical structure of fibers enables fiber-based devices to exhibit flexibility in multiple directions, unlike planar-based components. To demonstrate the structural advantage, bending tests were conducted in multiple directions, confirming their flexibility not only in the normal direction but also in various other directions (Figure S13).

Figure 5a illustrates the HLF fiber TFTs, connected to drive a fiber OLED that was reported in our previous work,[2] using a simple metal wiring connection. Although it was reported that the fiber phOLED using the dip-coating method showed high performance including low operating current (∼ a few 10^{-6} A) and voltage (<10 V), high luminance (over 10000 nit), and high flexibility (maximum tensile strain value of 1.75%), there have been no TFTs, which can drive the fiber phOLED, because of the aforementioned trade-off relationship between the electrical and mechanical properties. To demonstrate the fiber phOLED driven by the gate modulation, the metal wire between the fiber TFT and the fiber phOLED was connected by using commercial silver paste, as shown in Figure 5b (right). To drive a green fiber phOLED connected to the HLF fiber TFTs, a 4-probe Keithley system, a conventional electrical evaluation method for TFTs, was utilized (Figure 5b). It was driven by tipping directly to the electrode: GND to the source, V_g to the gate of the HLF fiber TFT, and V_{dd} to the anode of the green fiber phOLED, respectively. Figure 5c,d shows the luminance performance of the green fiber phOLED together with the output and transfer characteristics, representing the electrical performance of the HLF fiber TFTs. This allowed the performance of the OLED in the actual switching device to be evaluated. The green fiber phOLED was driven by the drain current resulting from the gate voltage sweep when a V_{DS} = 10 V bias of the saturation region was applied. The turn-on started from ∼10^{-6} A at V_{GS} = 1 V, and the maximum on-current was ∼10^{-4} A. Figure 5e shows that the fiber phOLED driving using the TFT was successfully operated, by confirming that the amount of light from the green fiber phOLED changes and switched with each voltage while performing a V_{GS} sweep (Movie S1). Additionally, to showcase the versatility and potential integration of multiple TFTs implemented in a single fiber, two OLED fibers were successfully combined with two TFTs, enabling them to be driven and operated (Figure S14).

The results demonstrated that the proposed HLF fiber TFT drove the fiber OLED, as a starting point for realizing fiber-based active-matrix organic light-emitting diodes (AMOLEDs). However, it seems that a more advanced technology is needed to implement a human-friendly wearable textile display (WTD), such as an addressable scheme and device structures for the drive. In particular, overall integration schemes, such as a fiber-based OLED-TFT with drive schemes, that can be more effectively incorporated into fabric are necessary beyond the fundamental technologies including fiber OLEDs and fiber TFTs. Also, there is still room for improvement, such as flexible encapsulation, which would ensure the passivation and washing characteristics of the WTD.

3. CONCLUSIONS

In summary, 1D cylindrical shaped fiber based IGZO TFTs were implemented which simultaneously exhibited high electrical performance and flexibility at a low process temperature of 150 °C. To address the trade-off relationship between the electrical and mechanical properties of the flexible fiber-based TFTs, four key process stages were designed: (I) a prethermal treatment that addressed alignment and the planarization effect, (II) partially patterned layers that were suitable structures for the cylindrical fiber, providing high performance, (III) a coplanar structure that served as the ohmic contact between the IGZO/Al interface, and (IV) an essentially novel CPA process that controlled the cooling process, enabling the films to maintain reliability. As a result, the HLF fiber TFTs exhibited a saturation mobility of 8.6 $cm^2/(V\ s)$ capable of driving an FHD display with a frame rate of 240 Hz or higher, and an excellent on/off ratio of 7.05 × 10^7, SS of 201 mV/dec, and low off current (∼10^{-12} A). At the

https://doi.org/10.1021/acsami.4c12223
ACS Appl. Mater. Interfaces 2024, 16, 62335−62346

same time, it was confirmed that the HLF fiber TFTs exhibit flexibility through a 0.6% strain, 1000 cycles tensile bending test. Furthermore, it was demonstrated that the HLF fiber TFT can drive a green fiber phOLED using a simple connection with Cu wiring and a Ag paste contact. The fiber phOLED was successfully modulated by the V_{GS} sweep of the HLF fiber TFT. Since active matrix organic light emitting diode (AMOLED) displays should be implemented with TFTs with high mobility and low off-current, it is believed that the proposed flexible fiber-based TFTs with high performance will be the starting point for realizing fiber-based AMOLED displays.

4. EXPERIMENTAL SECTION

4.1. Device Fabrication. *4.1.1. Fiber-Based TFTs.* The fiber-based IGZO TFTs were fabricated on a 500 μm diameter PET monofilament fiber with a top-gate/bottom-contact structure. The substrate was ultrasonically cleaned using methyl alcohol and deionized water for 5 min in each solution. To thermally contract the PET fiber, preannealing was performed at 150 °C for 5 min on a hot plate. To create a pattern on a cylindrical substrate with a fine feature size (<200 μm), we applied a shadow mask patterning method to all layers except the gate insulator layer. The gate insulator layer was formed using thermal atomic layer deposition (ALD) along the curved surface of the fiber without patterning. To minimize the shadow effect generated at the edge of the pattern, a flexible shadow mask made of a thin Cr material with a thickness of 0.05 mm was adhered to the fiber substrate. The thin film patterns using shadow masks was implemented with a microscope-equipped aligner equipment, thermal evaporator, and sputtering equipment. A thin film of 40 nm thick a-IGZO (In:Ga:Zn = 1:1:1 atom %) was deposited by radio frequency (RF) sputtering onto the PET fiber to form the active layer at room temperature. The RF power, pressure, and partial oxygen pressure (P_{O_2}) were 100 W, 5 mTorr, and 3%, respectively. The Al 50 nm source/drain and gate electrodes were deposited under the same conditions by thermal evaporation. The Al_2O_3 60 nm as the gate dielectric layer was deposited by thermal ALD using trimethyaluminum (TMA) as a precursor and H_2O as a reactant (LUCID D100, NCD Inc.). The Al_2O_3 thin film was grown in a 150 °C vacuum chamber. After deposition of the dielectric layer, postannealing was continuously conducted for 2 h in an ALD vacuum chamber.

4.1.2. Green Fiber phOLED. The fiber OLED was fabricated following the process reported in previous works.[2] A 300 μm diameter PET fiber was cleaned with isopropyl alcohol and deionized water in an ultrasonically cooled bath for 5 min. All solution processes were performed in a N_2 atmosphere at ∼100 °C. PEDOT:PSS (a cathode layer) was dip-coated six times at a withdrawal speed of 0.7 mm s^{-1}. ZnO NPs (as an electron injection layer) were dip-coated on the PET fiber at a rate of 10 mm s^{-1}. Next, polyethylenimine (PEI), which was diluted in 99.6 wt % 2-methoxyethanol, was dip-coated on the ZnO NP-coated fiber. Finally, the green EML solution was dip-coated at 50 mm s^{-1}. After the solution processes, a 4,4′,4″-tris(*N*-carbazolyl)-triphenylamine (TCTA) 40 nm, a molybdenum oxide (MoO_3) 10 nm, and a Al 100 nm layer were deposited by thermal evaporation vacuum (5×10^{-6} Torr) deposition.

4.2. Device Characterization. The transfer characteristics and output characteristics of the TFTs were measured by using a Keithley 4200-SCS in air. The surface roughness of the PET fiber was investigated by an AFM (XE-100) at room temperature. A cross section of the thin film on the fiber was SEM-photographed by using a focused ion beam (FIB) measurement (Helios Nanolab 450 F1) to confirm the difference in thickness according to the curvature of the fiber. XPS was conducted to analyze the surface and inside chemical composition of the IGZO thin film. To test the flexibility of the fiber based IGZO TFTs, the devices were bent in the direction of tensile stress with a bending strain of 0.6% (cyclic bending machine (Sciencetown Inc.)). For current density−voltage-luminance (*J*−*V*−*L*) measurement, the measurement system, including a source meter (2400 series, Keithley Inc.) equipped with a close-up lens (CS-A35) and a spectroradiometer (CS2000, Konica Minolta Inc.), were used. To analyze the mechanical properties of the proposed fiber TFT, FEA simulations based on the ANSYS mechanical simulator were conducted. The source of the fiber-based TFTs and the anode of the fiber OLED were connected with Cu wire from the outside using silver paste. They were measured by using a Keithley 4200-SCS apparatus and driven by tipping 3 parts: the drain, the gate of the fiber-based TFTs, and the cathode of the fiber OLED.

■ ASSOCIATED CONTENT

Supporting Information

The Supporting Information is available free of charge at https://pubs.acs.org/doi/10.1021/acsami.4c12223.

Photograph of PET fiber before and after preannealing, optical microscopy images and transfer characteristics of miss-aligned HLF-fiber TFTs without and with preannealing and successfully manufactured HLF-fiber TFTs with preannealing and tables, schematics of a 500 μm thick PET fiber with a fully deposited Al thin-film and cross-sectional SEM images showing the thickness of the single side deposited Al thin film versus the PET fiber position, TMA curves of glass transition of no treatment and furnace and CPA thermally treated 500 um PET fiber, annealing temperature versus annealing time to compare the CPA process and conventional TFT process, transfer characteristics of 5 HLF TFTs based on glass and PET fiber fabricated on different days to show the reproducibility, XRD results of IGZO thin film, thermally vacuum annealed IGZO thin film, and CPA processed IGZO/Al_2O_3 thin film, atomic percent versus etch time of XPS depth profiles measured at 20 nm thick IGZO film on PET, C 1s level spectra according to etch time = 360 s, PBS and NBS test results of HLF fiber based TFTs, photograph of the tensile bending test system, XPS O 1s peaks and deconvoluted peaks (no bending condition and 0.6% tensile strain, 2000 cycles of bending of the structure comprising 40 nm IGZO/500 μm PET fibers), comparison of the performance of the device without the CPA process (the common furnace process) before and after bending, stress distribution of a cylindrical fiber when bent (equations, simulation, and electrical properties of the fiber TFT when bent at various angles) (PDF)

Simple woven system of two OLEDs implemented on a single fiber, each driven by two TFTs (MP4)

■ AUTHOR INFORMATION

Corresponding Author

Kyung Cheol Choi − *School of Electrical Engineering, Korea Advanced Institute of Science and Technology (KAIST), Daejeon 34141, Republic of Korea;* orcid.org/0000-0001-6483-9516; Phone: +82-42-350-3482; Email: kyungcc@kaist.ac.kr; Fax: +82-42-350-8082

Authors

Chan Young Kim − *School of Electrical Engineering, Korea Advanced Institute of Science and Technology (KAIST), Daejeon 34141, Republic of Korea*

Yong Ha Hwang − *School of Electrical Engineering, Korea Advanced Institute of Science and Technology (KAIST), Daejeon 34141, Republic of Korea*

Jaehyeock Chang − *School of Electrical Engineering, Korea Advanced Institute of Science and Technology (KAIST), Daejeon 34141, Republic of Korea*

Seong Uk Kong − *School of Electrical Engineering, Korea Advanced Institute of Science and Technology (KAIST), Daejeon 34141, Republic of Korea*

Sang-Hee Ko Park − *Department of Materials Science and Engineering, Korea Advanced Institute of Science and Technology (KAIST), Daejeon 34141, Republic of Korea;* orcid.org/0000-0001-7165-8211

Complete contact information is available at: https://pubs.acs.org/10.1021/acsami.4c12223

Author Contributions

C.Y.K. and Y.H.H. contributed equally to this work.

Notes

The authors declare no competing financial interest.

■ ACKNOWLEDGMENTS

This work was supported by the Technology Innovation Program (20018379, Development of high-reliability light-emitting fiber-based woven wearable displays) funded By the Ministry of Trade, Industry & Energy (MOTIE, Korea). This work was supported by the Technology Innovation Program (20017569, Development of substrate materials that can be stretched more than 50% for stretchable displays) funded by the Ministry of Trade, Industry & Energy (MOTIE, Korea). This work was supported by project for materials, parts and equipment strategic cooperation R&D funded Korea Ministry of SMEs and Startups in 2022 (2022-00165409). This research was supported by National R&D Program through the National Research Foundation of Korea (NRF) funded by Ministry of Science and ICT (2021M3C1C3097646). The authors would like to acknowledge the technical support from ANSYS Korea.

■ REFERENCES

(1) Kwon, S.; Hwang, Y. H.; Nam, M.; Chae, H.; Lee, H. S.; Jeon, Y.; Lee, S.; Kim, C. Y.; Choi, S.; Jeong, E. G.; Choi, K. C. Recent Progress of Fiber Shaped Lighting Devices for Smart Display Applications—A Fibertronic Perspective. *Adv. Mater.* **2020**, *32* (5), 1−25.

(2) Hwang, Y. H.; Kwon, S.; Shin, J. B.; Kim, H.; Son, Y. H.; Lee, H. S.; Noh, B.; Nam, M.; Choi, K. C. Bright-Multicolor, Highly Efficient, and Addressable Phosphorescent Organic Light-Emitting Fibers: Toward Wearable Textile Information Displays. *Adv. Funct. Mater.* **2021**, *31* (18), 2009336.

(3) Hwang, Y. H.; Noh, B.; Lee, J.; Lee, H. S.; Park, Y.; Choi, K. C. High-Performance and Reliable White Organic Light-Emitting Fibers for Truly Wearable Textile Displays. *Adv. Sci.* **2022**, *9* (11), 1−10.

(4) Hwang, Y. H.; Kong, S. U.; Kim, C. Y.; Lee, J.; Cho, H. E.; Jeong, S. Y.; Choi, K. C. Organic Light-Emitting Fibers and Fabrics for Truly Wearable Smart Displays: Recent Progress and Future Opportunities. *J. Soc. Inf. Dispersion* **2022**, *30* (10), 727−747.

(5) Zhang, Z.; Cui, L.; Shi, X.; Tian, X.; Wang, D.; Gu, C.; Chen, E.; Cheng, X.; Xu, Y.; Hu, Y.; Zhang, J.; Zhou, L.; Fong, H. H.; Ma, P.; Jiang, G.; Sun, X.; Zhang, B.; Peng, H. Textile Display for Electronic and Brain-Interfaced Communications. *Adv. Mater.* **2018**, *30* (18), 1−8.

(6) Chen, G.; Li, Y.; Bick, M.; Chen, J. Smart Textiles for Electricity Generation. *Chem. Rev.* **2020**, *120* (8), 3668−3720.

(7) Weng, W.; Chen, P.; He, S.; Sun, X.; Peng, H. Smart Electronic Textiles. *Angew. Chemie - Int. Ed.* **2016**, *55* (21), 6140−6169.

(8) Shi, J.; Liu, S.; Zhang, L.; Yang, B.; Shu, L.; Yang, Y.; Ren, M.; Wang, Y.; Chen, J.; Chen, W.; Chai, Y.; Tao, X. Smart Textile-Integrated Microelectronic Systems for Wearable Applications. *Adv. Mater.* **2020**, *32* (5), 1−37.

(9) Carey, T.; Cacovich, S.; Divitini, G.; Ren, J.; Mansouri, A.; Kim, J. M.; Wang, C.; Ducati, C.; Sordan, R.; Torrisi, F. Fully Inkjet-Printed Two-Dimensional Material Field-Effect Heterojunctions for Wearable and Textile Electronics. *Nat. Commun.* **2017**, *8* (1), 1202.

(10) Park, J. W.; Kwon, S.; Kwon, J. H.; Kim, C. Y.; Choi, K. C. Low-Leakage Fiber-Based Field-Effect Transistors with an Al2O3-MgO Nanolaminate as Gate Insulator. *ACS Appl. Electron. Mater.* **2019**, *1* (8), 1400−1407.

(11) Kwon, S.; Kim, H.; Choi, S.; Jeong, E. G.; Kim, D.; Lee, S.; Lee, H. S.; Seo, Y. C.; Choi, K. C. Weavable and Highly Efficient Organic Light-Emitting Fibers for Wearable Electronics: A Scalable. *Low-Temperature Process. Nano Lett.* **2018**, *18* (1), 347−356.

(12) Kim, S. J.; Kim, H.; Ahn, J.; Hwang, D. K.; Ju, H.; Park, M. C.; Yang, H.; Kim, S. H.; Jang, H. W.; Lim, J. A. A New Architecture for Fibrous Organic Transistors Based on a Double-Stranded Assembly of Electrode Microfibers for Electronic Textile Applications. *Adv. Mater.* **2019**, *31* (23), 1−10.

(13) Kim, H. M.; Kang, H. W.; Hwang, D. K.; Lim, H. S.; Ju, B. K.; Lim, J. A. Metal-Insulator-Semiconductor Coaxial Microfibers Based on Self-Organization of Organic Semiconductor:Polymer Blend for Weavable, Fibriform Organic Field-Effect Transistors. *Adv. Funct. Mater.* **2016**, *26* (16), 2706−2714.

(14) Wang, H.; Zhang, Y.; Liang, X.; Zhang, Y. Smart Fibers and Textiles for Personal Health Management. *ACS Nano* **2021**, *15* (8), 12497−12508.

(15) Park, C. J.; Heo, J. S.; Kim, K. T.; Yi, G.; Kang, J.; Park, J. S.; Kim, Y. H.; Park, S. K. 1-Dimensional Fiber-Based Field-Effect Transistors Made by Low-Temperature Photochemically Activated Sol-Gel Metal-Oxide Materials for Electronic Textiles. *RSC Adv.* **2016**, *6* (22), 18596−18600.

(16) Jang, J.; Nam, S.; Hwang, J.; Park, J. J.; Im, J.; Park, C. E.; Kim, J. M. Photocurable Polymer Gate Dielectrics for Cylindrical Organic Field-Effect Transistors with High Bending Stability. *J. Mater. Chem.* **2012**, *22* (3), 1054−1060.

(17) Heo, J. S.; Kim, T.; Ban, S. G.; Kim, D.; Lee, J. H.; Jur, J. S.; Kim, M. G.; Kim, Y. H.; Hong, Y.; Park, S. K. Thread-Like CMOS Logic Circuits Enabled by Reel-Processed Single-Walled Carbon Nanotube Transistors via Selective Doping. *Adv. Mater.* **2017**, *29* (31), 1−8.

(18) Lee, J.; Ihle, S. J.; Pellegrino, G. S.; Kim, H.; Yea, J.; Jeon, C. Y.; Son, H. C.; Jin, C.; Eberli, D.; Schmid, F.; Zambrano, B. L.; Renz, A. F.; Forró, C.; Choi, H.; Jang, K. I.; Küng, R.; Vörös, J. Stretchable and Suturable Fibre Sensors for Wireless Monitoring of Connective Tissue Strain. *Nat. Electron.* **2021**, *4* (4), 291−301.

(19) Guan, F.; Xie, Y.; Wu, H.; Meng, Y.; Shi, Y.; Gao, M.; Zhang, Z.; Chen, S.; Chen, Y.; Wang, H.; Pei, Q. Silver Nanowire-Bacterial Cellulose Composite Fiber-Based Sensor for Highly Sensitive Detection of Pressure and Proximity. *ACS Nano* **2020**, *14* (11), 15428−15439.

(20) Liao, M.; Wang, C.; Hong, Y.; Zhang, Y.; Cheng, X.; Sun, H.; Huang, X.; Ye, L.; Wu, J.; Shi, X.; Kang, X.; Zhou, X.; Wang, J.; Li, P.; Sun, X.; Chen, P.; Wang, B.; Wang, Y.; Xia, Y.; Cheng, Y.; Peng, H. Industrial Scale Production of Fibre Batteries by a Solution-Extrusion Method. *Nat. Nanotechnol.* **2022**, *17* (4), 372−377.

(21) He, J.; Lu, C.; Jiang, H.; Han, F.; Shi, X.; Wu, J.; Wang, L.; Chen, T.; Wang, J.; Zhang, Y.; Yang, H.; Zhang, G.; Sun, X.; Wang, B.; Chen, P.; Wang, Y.; Xia, Y.; Peng, H. Scalable Production of High-Performing Woven Lithium-Ion Fibre Batteries. *Nature* **2021**, *597* (7874), 57−63.

(22) Jang, Y.; Kim, S. M.; Spinks, G. M.; Kim, S. J. Carbon Nanotube Yarn for Fiber-Shaped Electrical Sensors, Actuators, and Energy Storage for Smart Systems. *Adv. Mater.* **2020**, *32* (5), 1−14.

(23) You, M. H.; Wang, X. X.; Yan, X.; Zhang, J.; Song, W. Z.; Yu, M.; Fan, Z. Y.; Ramakrishna, S.; Long, Y. Z. A Self-Powered Flexible Hybrid Piezoelectric-Pyroelectric Nanogenerator Based on Non-Woven Nanofiber Membranes. *J. Mater. Chem. A* **2018**, *6* (8), 3500−3509.

(24) Bonfiglio, A.; De Rossi, D.; Kirstein, T.; Locher, I. R.; Mameli, F.; Paradiso, R.; Vozzi, G. Organic Field Effect Transistors for Textile Applications. *IEEE Trans. Inf. Technol. Biomed.* **2005**, *9* (3), 319−324.
(25) Bae, H.; Jang, B. C.; Park, H.; Jung, S. H.; Lee, H. M.; Park, J. Y.; Jeon, S. B.; Son, G.; Tcho, I. W.; Yu, K.; Im, S. G.; Choi, S. Y.; Choi, Y. K. Functional Circuitry on Commercial Fabric via Textile-Compatible Nanoscale Film Coating Process for Fibertronics. *Nano Lett.* **2017**, *17* (10), 6443−6452.
(26) Zou, S. J.; Shen, Y.; Xie, F. M.; Chen, J. De; Li, Y. Q.; Tang, J. X. Recent Advances in Organic Light-Emitting Diodes: Toward Smart Lighting and Displays. *Mater. Chem. Front.* **2020**, *4* (3), 788−820.
(27) Li, P.; Gao, X.; Zhao, B.; Pan, K.; Deng, J. Multi-Color Tunable and White Circularly Polarized Luminescent Composite Nanofibers Electrospun from Chiral Helical Polymer. *Adv. Fiber Mater.* **2022**, *4* (6), 1632−1644.
(28) Hu, X.; Xu, Y.; Wang, J.; Ma, J.; Wang, L.; Jiang, W. In Situ Fabrication of Superfine Perovskite Composite Nanofibers with Ultrahigh Stability by One-Step Electrospinning Toward White Light-Emitting Diode. *Adv. Fiber Mater.* **2023**, *5* (1), 183−197.
(29) Shi, X.; Zuo, Y.; Zhai, P.; Shen, J.; Yang, Y.; Gao, Z.; Liao, M.; Wu, J.; Wang, J.; Xu, X.; Tong, Q.; Zhang, B.; Wang, B.; Sun, X.; Zhang, L.; Pei, Q.; Jin, D.; Chen, P.; Peng, H. Large-Area Display Textiles Integrated with Functional Systems. *Nature* **2021**, *591* (7849), 240−245.
(30) Song, Y. J.; Kim, J.-W.; Cho, H.-E.; Son, Y. H.; Lee, M. H.; Lee, J.; Choi, K. C.; Lee, S.-M. Fibertronic Organic Light-Emitting Diodes toward Fully Addressable, Environmentally Robust. *Wearable Displays. ACS Nano* **2020**, *14* (1), 1133−1140.
(31) Song, H.; Song, Y. J.; Hong, J.; Kang, K. S.; Yu, S.; Cho, H. E.; Kim, J. H.; Lee, S. M. Water Stable and Matrix Addressable OLED Fiber Textiles for Wearable Displays with Large Emission Area. *npj Flex. Electron.* **2022**, *6* (1), 1−8.
(32) Kim, C. Y.; Park, J. H.; Park, S. H. K.; Choi, K. C. High-Mobility IGZO Thin-Film Transistors Fabricated on a Flexible PET Monofilament Fiber for Wearing Display. *Dig. Technol. Pap. - SID Int. Symp.* **2020**, *51* (1), 1822−1824.
(33) Hwang, Y. H.; Kim, C. Y.; Kong, S. U.; Choi, K. C. High-Performance Fiber-Based Red Oleds and Tfts for Truly Wearable Textile Displays. *Dig. Technol. Pap. - SID Int. Symp.* **2022**, *53* (1), 577−580.
(34) Rembert, T.; Battaglia, C.; Anders, A.; Javey, A. Room Temperature Oxide Deposition Approach to Fully Transparent, All-Oxide Thin-Film Transistors. *Adv. Mater.* **2015**, *27* (40), 6090−6095.
(35) Nomura, K.; Ohta, H.; Takagi, A.; Kamiya, T.; Hirano, M.; Hosono, H. Room-Temperature Fabrication of Transparent Flexible Thin-Film Transistors Using Amorphous Oxide Semiconductors. *Nature* **2004**, *432* (7016), 488−492.
(36) Liu, X.; Wang, C.; Cai, B.; Xiao, X.; Guo, S.; Fan, Z.; Li, J.; Duan, X.; Liao, L. Rational Design of Amorphous Indium Zinc Oxide/Carbon Nanotube Hybrid Film for Unique Performance Transistors. *Nano Lett.* **2012**, *12* (7), 3596−3601.
(37) Lee, H. E.; Kim, S.; Ko, J.; Yeom, H. I.; Byun, C. W.; Lee, S. H.; Joe, D. J.; Im, T. H.; Park, S. H. K.; Lee, K. J. Skin-Like Oxide Thin-Film Transistors for Transparent Displays. *Adv. Funct. Mater.* **2016**, *26* (34), 6170−6178.
(38) Sheng, J.; Jeong, H. J.; Han, K. L.; Hong, T. H.; Park, J. S. Review of Recent Advances in Flexible Oxide Semiconductor Thin-Film Transistors. *J. Inf. Dispersion* **2017**, *18* (4), 159−172.
(39) Liu, C.; Minari, T.; Xu, Y.; Yang, B. R.; Chen, H. X.; Ke, Q.; Liu, X.; Hsiao, H. C.; Lee, C. Y.; Noh, Y. Y. Direct and Quantitative Understanding of the Non-Ohmic Contact Resistance in Organic and Oxide Thin-Film Transistors. *Org. Electron.* **2015**, *27*, 253−258.
(40) Chen, J.; Ning, H.; Fang, Z.; Tao, R.; Yang, C.; Zhou, Y.; Yao, R.; Xu, M.; Wang, L.; Peng, J. Reduced Contact Resistance of A-IGZO Thin Film Transistors with Inkjet-Printed Silver Electrodes. *J. Phys. D. Appl. Phys.* **2018**, *51* (16), 165103.
(41) García-Valenzuela, J. A.; Rivera, R.; Morales-Vilches, A. B.; Gerling, L. G.; Caballero, A.; Asensi, J. M.; Voz, C.; Bertomeu, J.; Andreu, J. Main Properties of Al2O3 Thin Films Deposited by Magnetron Sputtering of an Al2O3 Ceramic Target at Different Radio-Frequency Power and Argon Pressure and Their Passivation Effect on p-Type c-Si Wafers. *Thin Solid Films* **2016**, *619*, 288−296.
(42) Kim, H. K.; Kim, D. G.; Lee, K. S.; Huh, M. S.; Jeong, S. H.; Kim, K. I.; Kim, H.; Han, D. W.; Kwon, J. H. Plasma Damage-Free Deposition of Al Cathode on Organic Light-Emitting Devices by Using Mirror Shape Target Sputtering. *Appl. Phys. Lett.* **2004**, *85* (19), 4295−4298.
(43) Park, J. S.; Maeng, W. J.; Kim, H. S.; Park, J. S. Review of Recent Developments in Amorphous Oxide Semiconductor Thin-Film Transistor Devices. *Thin Solid Films* **2012**, *520* (6), 1679−1693.
(44) Yonebayashi, R.; Tanaka, K.; Okada, K.; Yamamoto, K.; Yamamoto, K.; Uchida, S.; Aoki, T.; Takeda, Y.; Furukawa, H.; Ito, K.; Katoh, H.; Nakamura, W. High Refresh Rate and Low Power Consumption AMOLED Panel Using Top-Gate n-Oxide and p-LTPS TFTs. *J. Soc. Inf. Dispersion* **2020**, *28* (4), 350−359.
(45) Ahnood, A.; Ghaffarzadeh, K.; Nathan, A.; Servati, P.; Li, F.; Esmaeili-Rad, M. R.; Sazonov, A. Non-Ohmic Contact Resistance and Field-Effect Mobility in Nanocrystalline Silicon Thin Film Transistors. *Appl. Phys. Lett.* **2008**, *93* (16), 163503.
(46) Servati, P.; Striakhilev, D.; Nathan, A. Above-Threshold Parameter Extraction and Modeling for Amorphous Silicon Thin-Film Transistors. *IEEE Trans. Electron Devices* **2003**, *50* (11), 2227−2235.
(47) Yeo, J.; Kim, G.; Hong, S.; Kim, M. S.; Kim, D.; Lee, J.; Lee, H. B.; Kwon, J.; Suh, Y. D.; Kang, H. W.; Sung, H. J.; Choi, J. H.; Hong, W. H.; Ko, J. M.; Lee, S. H.; Choa, S. H.; Ko, S. H. Flexible Supercapacitor Fabrication by Room Temperature Rapid Laser Processing of Roll-to-Roll Printed Metal Nanoparticle Ink for Wearable Electronics Application. *J. Power Sources* **2014**, *246*, 562−568.
(48) Lyu, M. Y. Effect of Annealing Conditions on Thermal Properties and Crystallization Behavior of Poly(Ethylene Terephthalate). *Int. Polym. Process.* **2010**, *25* (2), 118−124.
(49) Nguyen, C. P. T.; Raja, J.; Kim, S.; Jang, K.; Le, A. H. T.; Lee, Y. J.; Yi, J. Enhanced Electrical Properties of Oxide Semiconductor Thin-Film Transistors with High Conductivity Thin Layer Insertion for the Channel Region. *Appl. Surf. Sci.* **2017**, *396*, 1472−1477.
(50) Raja, J.; Jang, K.; Nguyen, H. H.; Trinh, T. T.; Choi, W.; Yi, J. Enhancement of Electrical Stability of A-IGZO TFTs by Improving the Surface Morphology and Packing Density of Active Channel. *Curr. Appl. Phys.* **2013**, *13* (1), 246−251.
(51) Cantwell, W. J.; Davies, P.; Kausch, H. H. The Effect of Cooling Rate on Deformation and Fracture in IM6/PEEK Composites. *Compos. Struct.* **1990**, *14* (2), 151−171.
(52) Oshima, S.; Higuchi, R.; Kato, M.; Minakuchi, S.; Yokozeki, T.; Aoki, T. Experimental Data for Cooling Rate-Dependent Properties of Polyphenylene Sulfide (PPS) and Carbon Fiber Reinforced PPS (CF/PPS). *Data Br.* **2023**, *46*, No. 108817.
(53) Groeninckx, G.; Reynaers, H. Morphology and Melting Behavior of Semicrystalline Poly(Ethylene Terephthalate) - 2. Annealed Pet. *J. Polym. Sci. Part A-2, Polym. Phys.* **1980**, *18* (6), 1325−1341.
(54) Kamiya, T.; Nomura, K.; Hosono, H. Present Status of Amorphous In-Ga-Zn-O Thin-Film Transistors. *Sci. Technol. Adv. Mater.* **2010**, *11* (4), 044305.
(55) Benson, S. W. Papers — III Bond Energies. *J. Chem. Educ.* **1965**, *42* (9), 502−518.
(56) Nam, Y.; Kim, H. O.; Cho, S. H.; Ko Park, S. H. Effect of Hydrogen Diffusion in an In-Ga-Zn-O Thin Film Transistor with an Aluminum Oxide Gate Insulator on Its Electrical Properties. *RSC Adv.* **2018**, *8* (10), 5622−5628.
(57) Parthiban, S.; Park, K.; Kim, H. J.; Yang, S.; Kwon, J. Y. Carbon-Incorporated Amorphous Indium Zinc Oxide Thin-Film Transistors. *J. Electron. Mater.* **2014**, *43* (11), 4224−4228.
(58) Yoo, H.; Tak, Y. J.; Kim, W. G.; Kim, Y. G.; Kim, H. J. A Selectively Processible Instant Glue Passivation Layer for Indium Gallium Zinc Oxide Thin-Film Transistors Fabricated at Low Temperature. *J. Mater. Chem. C* **2018**, *6* (23), 6187−6193.

https://doi.org/10.1021/acsami.4c12223
ACS Appl. Mater. Interfaces 2024, 16, 62335−62346

(59) Kim, J.; Jeong, S. M.; Jeong, J. Transparent Thin-Film Transistor and Diode Circuit Using Graphene and Amorphous Indium-Gallium-Zinc-Oxide Active Layer. *Electron. Lett.* **2015**, *51* (24), 2047−2049.
(60) Jen, S. H.; Bertrand, J. A.; George, S. M. Critical Tensile and Compressive Strains for Cracking of Al 2O3 Films Grown by Atomic Layer Deposition. *J. Appl. Phys.* **2011**, *109* (8), 084305.
(61) Sheng, J.; Park, J.; Choi, D.-w.; Lim, J.; Park, J.-S. A Study on the Electrical Properties of Atomic Layer Deposition Grown InOx on Flexible Substrates with Respect to N2O Plasma Treatment and the Associated Thin-Film Transistor Behavior under Repetitive Mechanical Stress. *ACS Appl. Mater. Interfaces* **2016**, *8* (45), 31136−31143.
(62) Hamedi, M.; Forchheimer, R.; Inganäs, O. Towards Woven Logic from Organic Electronic Fibres. *Nat. Mater.* **2007**, *6* (5), 357−362.
(63) Muller, C.; Hamedi, M.; Karlsson, R.; Jansson, R.; Marcilla, R.; Hedhammar, M.; Inganas, O. Woven Electrochemical Transistors on Silk Fibers. *Adv. Mater.* **2011**, *23* (7), 898−901.
(64) Lee, J. B.; Subramanian, V. On Fiber for E-Textiles. *Science (80-.).* **2005**, *52* (2), 269−275.
(65) Lee, W.; Kim, Y.; Lee, M. Y.; Oh, J. H.; Lee, J. U. Highly Stretchable Fiber Transistors with All-Stretchable Electronic Components and Graphene Hybrid Electrodes. *Org. Electron.* **2019**, *69*, 320−328.

https://doi.org/10.1021/acsami.4c12223
ACS Appl. Mater. Interfaces 2024, 16, 62335−62346